

Multiqubit Toffoli Gates and Optimal Geometry with Rydberg Atoms

Dongmin Yu,^{1,†} Han Wang,^{1,‡} Jin-Ming Liu^{1,§}, Shi-Lei Su,^{2,*} Jing Qian^{1,5,‡} and Weiping Zhang^{1,3,4,5,6}

¹*State Key Laboratory of Precision Spectroscopy, Department of Physics, School of Physics and Electronic Science, East China Normal University, Shanghai 200241, China*

²*School of Physics, Zhengzhou University, Zhengzhou 450001, China*

³*School of Physics and Astronomy, and Tsung-Dao Lee Institute, Shanghai Jiao Tong University, Shanghai 200240, China*

⁴*Shanghai Research Center for Quantum Sciences, Shanghai 201315, China*

⁵*Shanghai Branch, Heifei National Laboratory, Shanghai 201315, China*

⁶*Collaborative Innovation Center of Extreme Optics, Shanxi University, Taiyuan, Shanxi 030006, China*

(Received 28 February 2022; revised 22 May 2022; accepted 22 August 2022; published 27 September 2022)

Due to its potential for implementing a scalable quantum computer, the multiqubit Toffoli gate lies in the heart of quantum information processing. In this paper, we demonstrate a multiqubit blockade gate with atoms arranged in a three-dimensional spheroidal array. The gate performance is greatly improved by the method of optimizing control-qubit distributions on the spherical surface via evolutionary algorithm, which leads to an enhanced asymmetric Rydberg blockade. This spheroidal configuration, not only preserves the dipole blockade energy well between arbitrary control-target pairs, which keeps the asymmetric blockade error at a very low level, but also manifests an unprecedented robustness to the spatial position variations, leading to a negligible position error. Taking account of intrinsic errors and using typical experimental parameters, we numerically show that a C₆NOT Rydberg gate can be created with a fidelity of 0.992, which is only limited by the Rydberg state decays. Our protocol opens up a platform of higher-dimensional atomic arrays for achieving multiqubit neutral-atom quantum computation.

DOI: 10.1103/PhysRevApplied.18.034072

I. INTRODUCTION

Rydberg atoms serve as a reliable platform for studying quantum computing and quantum simulation because of their strong and tunable interactions, which can block the excitation of surrounding atoms in the vicinity of a preexcited atom [1–3]. Via this so-called Rydberg blockade mechanism, versatile quantum gates can be created [4–8], which manifest as basic logic calculation units for universal quantum computation [9,10]. Among existing Rydberg-mediated quantum gates, a multiqubit Toffoli (C_nNOT) gate is a useful family member, which can offer an efficient implementation of Grover quantum search algorithm to speedup the searches on a programmable quantum computer [11] or to extend into any dimensional quantum systems [12]. A conventional three-qubit Toffoli (C₂NOT) gate can be implemented in a one-dimensional (1D) array [13,14] where two outer control atoms constrain the behavior of the middle target atom with strong control-target interactions. However such a linear model

is unsuited for engineering a multiqubit gate because one target atom cannot be simultaneously manipulated by two nearest-neighbor control qubits due to the blockade mechanism [15]. Therefore previous contributions to a multiqubit Toffoli gate often rely on the assembly of several elementary gates [16–20] or the parallel operation on some clusters of atoms in a 1D array of optical tweezers [21]. Direct execution of multiqubit Toffoli gates ($n \geq 3$) remains a big challenge both in theory and experiment.

To date, several studies for multiqubit gates use the way of adiabatic passages in which the evolution of states can be performed by obeying a multiqubit dark eigenstate with complex optimal pulses [22,23]. An alternative way for this target depends on nonadiabatic holonomic quantum computation showing a C₃NOT gate with an error of 0.0018 [24]. Another prominent idea to the realization of multiqubit Rydberg gates adopts asymmetric blockade as proposed in Ref. [25], in which there exists a large separation of scales between different types of Rydberg interactions [26–29]. However we note that, the asymmetric interaction condition breaks easily when the number of qubits is enlarged, especially for atoms arranged in one-dimensional (1D) or two-dimensional (2D) arrays where distant control-target

*slsu@zzu.edu.cn

†Corresponding author: jqian1982@gmail.com

‡These authors contributed equally to this work.

interaction suffers from a dramatic decrease. Recently Young and coworkers propose a 2D multiqubit gate by placing many control and many target atoms at the same time, in which the strong control-control and control-target interactions can be engineered via extra microwave fields, leading to a perfect asymmetric blockade [29]. But this scheme is still unsuitable for implementing individual multicontrol [30–32] or multitarget [33] gates due to the absence of strong and tunable interactions between distant atoms.

In the present work, inspired by the development of defect-free atomic arrays from 2D to three-dimensional (3D) platforms where arbitrary atoms can be arranged expectantly in space [34–39] (a recent work has reported mixed-species atom arrays with arbitrary geometry [40]), we propose a scheme for implementing C_n NOT gates with atoms individually arranged in a 3D spheroidal atomic array. As illustrated in Fig. 1, we consider a single target atom (in green) located at the center and n control atoms (in red) on the surface. Such a 3D atomic array can be treated as an assembling of multilayer 2D lattices and easily achieve single-site Rydberg addressing [41]. Compared to the existing asymmetric-blockade-based protocols [25–29], our scheme benefits from an optimal 3D configuration to maximize the asymmetry of blockade, representing an unprecedented robustness to the 3D atomic position variations. The synthetic interplay between interatomic Rydberg-Rydberg interactions and the optimal geometry results in a huge asymmetric blockade, making the gate imperfection dominated by an intrinsic decay error, and the asymmetric blockade error can be suppressed to a negligible level. Our results show that a simple estimate of decay errors gives rise to an acceptable fidelity of 0.9537 for a multiqubit C_{12} NOT gate. This 3D Rydberg quantum gate can serve as an alternative gate unit for parallel operation in 3D optical tweezers, which is promising for scalable quantum computation with more flexibility.

II. MAXIMIZING ASYMMETRIC BLOCKADE VIA OPTIMIZATION

To achieve desirable asymmetric interactions we adopt optimization with an evolutionary algorithm. Since each atom contains two Rydberg states $|p_{j,t}\rangle$ and $|s_{j,t}\rangle$ with subscript $j(t)$ for the control (target) atom, we consider the interaction between atoms in product states $|p_j s_t\rangle$ and $|s_j p_t\rangle$ is of resonant dipole-dipole feature [42]

$$\hat{U}_{c_j t}(\theta_{c_j t}) = \frac{C_3^{sp}(\theta_{c_j t})}{R_{ct}^3} (|p_j s_t\rangle \langle s_j p_t| + |s_j p_t\rangle \langle p_j s_t|), \quad (1)$$

with $C_3^{sp}(\theta_{c_j t}) = C_3(1 - 3 \cos^2 \theta_{c_j t})$ and $C_3 = |\mu_{sp}|^2 / (8\pi\epsilon_0)$ (see Appendix A for more details). Note that the spheroidal structure can preserve the control-target

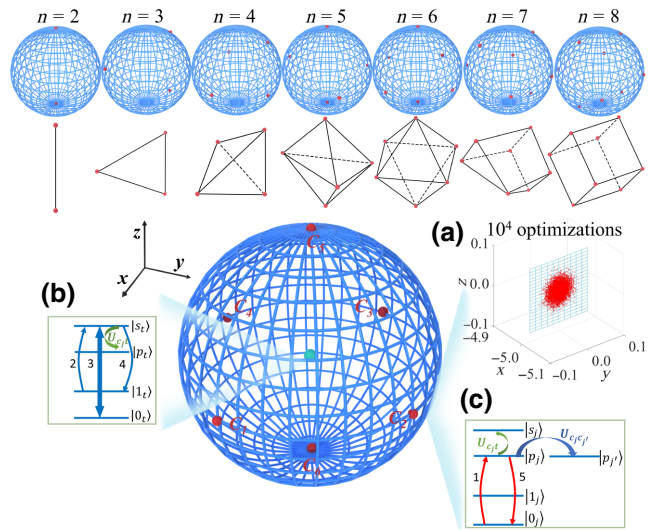


FIG. 1. Realization of spheroidal multiqubit Toffoli gates in a 3D atomic array. Upper panels: optimized distributions of n control atoms on the surface accompanied by the optimal geometries explicitly shown below. Main panel: amplification of the C_6 NOT gate with four control atoms c_{1-4} at the equatorial plane and two control atoms c_{5-6} at the south and north poles. The target atom is placed at the center. (a) Distribution of c_2 after 10^4 optimizations via evolutionary algorithm. (b),(c) The atomic energy levels as well as the atom-light interactions. In the presence of a static electric field, we fix the quantization axis along $+\hat{z}$ to simplify the optimization, which makes an angular-dependent dipole-dipole interaction $U_{c_j t}(\theta_{c_j t})$ arise for each control-target atomic pair, while the control-control interaction $U_{c_j c_{j'}}$ ($|\mathbf{r}_j - \mathbf{r}_{j'}|$) is of vdW type, which depends on the intraspecies distance $R_{c_j c_{j'}}$.

distance R_{ct} unchanged so $U_{c_j t}$ depends only on the polarizing angle $\theta_{c_j t}$. On the other hand there is also a van der Waals (vdW) interaction between two control atoms, given by [43]

$$\hat{U}_{c_j c_{j'}}(|\mathbf{r}_j - \mathbf{r}_{j'}|) = \frac{C_6}{R_{c_j c_{j'}}^6} |\mathbf{p}_j \mathbf{p}_{j'}\rangle \langle \mathbf{p}_j \mathbf{p}_{j'}|, \quad (2)$$

with $R_{c_j c_{j'}} = |\mathbf{r}_j - \mathbf{r}_{j'}|$ the control-control distance, which is a vdW energy shift of the pair state $|\mathbf{p}_j \mathbf{p}_{j'}\rangle$ considered arising from a second-order approximation of the nonresonant dipole-dipole interaction.

Below we focus on how to achieve the best asymmetric blockade using ^{87}Rb Rydberg states: $|s_{t,j}\rangle = |(m+1)S_{1/2}, m_j = 1/2\rangle$, $|p_{t,j}\rangle = |mP_{3/2}, m_j = 3/2\rangle$ as in Ref. [26]. The C_3 coefficient for $m = 60$ is about $C_3/2\pi = 4.194 \text{ GHz } \mu\text{m}^3$ and $C_6/2\pi = -12.0 \text{ GHz } \mu\text{m}^6$ calculated by the ARC open-source library [44]. Since $U_{c_j t} \propto (1 - 3 \cos^2 \theta_{c_j t})$ and $U_{c_j c_{j'}} \propto 1/R_{c_j c_{j'}}^6$, the condition of strongly asymmetric interactions $U_{c_j t} \gg U_{c_j c_{j'}}$, i.e., any control atom can block the excitation of the target atom without blocking other control atoms, can be readily met if $R_{c_j c_{j'}}$ is

appropriate. In Appendix B we verify the establishment of strong asymmetric interactions by calculating the leakage error due to nonresonant Rydberg couplings nearby. We also note that the asymmetry increases for small principal quantum number because the coefficient $C_3(C_6)$ scales as approximately m^4 (approximately m^{11}) [25]. Lowering m can realize a 3D quantum gate with more control qubits (details in Sec. V).

Here, in order to maximize asymmetric blockade, we have to optimize the spatial positions of all control atoms accompanied by a dipole-angle optimization. For arbitrary control atom c_j a factor characterizing asymmetry is defined as

$$\chi_j = U_{c_j t} / U_{c_j c_j}, \quad (3)$$

which must be maximized. Intuitively, by increasing n , the vdW interaction is enhanced so as to easily break the asymmetry. To determine the maximal n_{\max} permitted for a chosen radius R_{ct} (the scale of the 3D array), we perform a global optimization to the atomic positions via the evolutionary algorithm [45]. A detailed description of the optimization algorithm can be found in Appendix C. For achieving strong asymmetric blockade, we set $\chi_j > 100$, which means the minimal value of χ_j should satisfy $\min(\chi_j) > 100$ for any c_j . This limitation leads to $n_{\max} = 8$ when $R_{ct} = 5.0 \mu\text{m}$ and $m = 60$. Several optimal geometries are shown in Fig. 1(upper panels) where the positions of control atoms denoted as red dots, are precisely obtained by sufficient optimization. This optimal structure does not depend on the coefficients C_3 or C_6 chosen and is stably existing. For an even n value, the structure looks more regular. The physics behind these optimal geometries can be understood by seeking for a maximal asymmetry between dipole-dipole interaction and vdW interaction, where the potential energy of the system reaches its global minimum, corresponding to a maximal magnitude of dipole-dipole interaction. This specific geometry is formed by a competition between attractive vdW interactions and inhomogeneous dipole-dipole interactions, which is discussed in Appendix D. Figure 1(a) represents an amplified position distribution of c_2 under 10^4 optimization. They are extremely condensed in space, confirming the accuracy of the algorithm.

III. GATE PERFORMANCE AND DECAY ERROR

As examples we investigate the gate performance of an optimal 3D $C_6\text{NOT}$ gate. The effective non-Hermitian Hamiltonian including the dissipative dynamics, is expressed as

$$\hat{\mathcal{H}}_{\text{eff}} = \hat{\mathcal{H}}_0 + \hat{\mathcal{H}}_I - \frac{i}{2} \sum_k \hat{\mathcal{L}}_k^\dagger \hat{\mathcal{L}}_k, \quad (4)$$

with k the indices of Rydberg levels $|p_{j,j',t}\rangle$ and $|s_{j,t}\rangle$, and the Hamiltonians

$$\begin{aligned} \hat{\mathcal{H}}_0 = \frac{1}{2} \{ & \Omega_c \sum_j^n (|0_j\rangle\langle p_j| + |p_j\rangle\langle 0_j|) \\ & + \Omega_t [|1_t\rangle\langle s_t| + |s_t\rangle\langle 1_t| + (|0_t\rangle\langle s_t| + \text{H.c.})] \}, \end{aligned} \quad (5)$$

$$\hat{\mathcal{H}}_I = \sum_{j,j'>j} U_{c_j c_{j'}} + \sum_j U_{c_j t} \quad (6)$$

represent the atom-light couplings and the atom-atom Rydberg interactions. $\Omega_{c(t)}$ is the Rabi frequency for the control (target) atoms. To characterize the gate performance we calculate the average gate fidelity

$$\bar{\mathcal{F}}_n = \frac{1}{2^{n+1}} \text{Tr}\{[\sqrt{\rho_{et}}|\bar{\Psi}_{\text{out}}\rangle\langle\bar{\Psi}_{\text{out}}|\sqrt{\rho_{et}}]^{1/2}\} \quad (7)$$

by solving the stochastic Schrödinger equation subject to arbitrary computational basis $|\Psi\rangle$ [46]:

$$\partial_t |\Psi\rangle = -i\hat{\mathcal{H}}_{\text{eff}} |\Psi\rangle. \quad (8)$$

During each time interval δt , one generates a random number δp and compares it with the instantaneous population on Rydberg states. If δp is larger, the system will evolve by obeying the Schrödinger equation (8); otherwise one generates a random Rydberg excitation via a quantum jump [47]. The total random number is $t_{\text{det}}/\delta t$ where $t_{\text{det}} = 2\pi/\Omega_c + 3\pi/\Omega_t$ is the gate duration. By initializing 2^{n+1} input states, $\bar{\Psi}_{\text{out}}$ denotes the average output at $t = t_{\text{det}}$ after 500 stochastic evolutions and ρ_{et} is an etalon matrix. In addition, the operator

$$\hat{\mathcal{L}}_k = \sqrt{\Gamma_k} (|1\rangle\langle k| + |0\rangle\langle k|) \quad (9)$$

indicates the spontaneous population decay of Rydberg levels, in which the decay rates are $\Gamma_k = \Gamma_p$ for $k = p_{j,j',t}$ and $\Gamma_k = \Gamma_s$ for $k = s_{j,t}$.

By performing further calculations, for $n = 6$ we find $(\min(U_{c_j t}), \max(U_{c_j c_j})) / 2\pi = (33.552, 0.096)$ MHz, leading to the asymmetry: $\min(\chi_j) = 349.5 > 100$. Such a huge asymmetry can keep the intrinsic asymmetric error originating from imperfect control-target (control) (anti)blockade at a very low level $< 10^{-5}$. In turn we extend this asymmetric condition to a more generalized form, as

$$\min(U_{c_j t}), \Omega_c \gg \Omega_t \gg \max(U_{c_j c_j}), \quad (10)$$

which is also related to relevant pulse strengths [25]. Based on Eq. (10) we assume

$$\Omega_t = \min(U_{c_j t})/20, \Omega_c = 5 \min(U_{c_j t}) \quad (11)$$

throughout the paper. The decay rate is $\Gamma_s = 5.0 \text{ kHz}$ and $\Gamma_p = 3.4 \text{ kHz}$ in a cryogenic environment [48], we find a

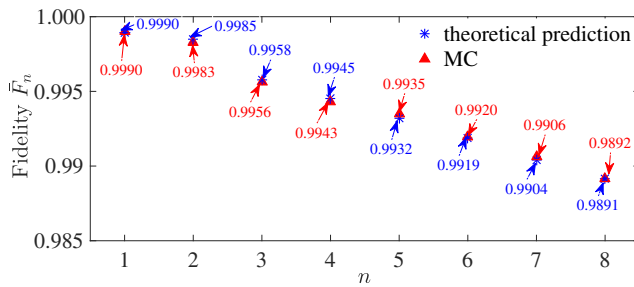


FIG. 2. Average gate fidelity $\bar{\mathcal{F}}_n$ as a function of the control atomic number n , estimated by the numerical Monte Carlo method (red triangles) and the theoretical expression (blue stars).

gate fidelity of $\bar{\mathcal{F}}_6 = 0.9920$, which is mainly constrained by the decay error from Rydberg levels [the decay error is about 8×10^{-3} estimated by Eq. (12)]. The overall gate time is $t_{\text{det}} \approx 3\pi/\Omega_t = 894$ ns. Detailed description of the gate operation can be found in Appendix E. In Fig. 2 we show that the average gate fidelity $\bar{\mathcal{F}}_n$ (red triangles and texts, estimated by MC) decreases with the control atom number n . For comparison, it is instructive to recall the decay-error expression [26]

$$\mathcal{E}_{n,\text{se}} = \frac{1}{2^n} \frac{\pi \Gamma_s}{\Omega_t} + n \frac{3\pi \Gamma_p}{2\Omega_t} + n \frac{\pi \Gamma_p}{2\Omega_c}, \quad (12)$$

by which the gate fidelity can be analytically obtained according to $\mathcal{F}_n \approx 1 - \mathcal{E}_{n,\text{se}}$ (blue stars and texts). A good agreement is observable between the theoretical and numerical predictions, which confirms that other intrinsic asymmetric errors including blockade error and antiblockade error, are both negligible due to the huge asymmetry in our scheme.

IV. RESILIENCE TO POSITION VARIATIONS

Owing to the finite temperature, which leads to atomic position variations in the optical trap, the interatomic interaction strength is slightly different for each measurement. This so-called *position error* could catastrophically break the implementation of Rydberg antiblockade- (RAB) based gates, which depend on a severely modified RAB condition [49–52]. Although the excitation annihilation as reviewed in Ref. [53] or transition slow-down effect [54] makes blockade gates benefited from a robustness against interaction fluctuations, most current achievements are still constrained to fewer-qubit gates [55,56] because the blockade strength decreases significantly for two distant atoms. Here we express the control (target) atom position as

$$\mathbf{r}_{j(t)} = \mathbf{r}_{0,j(t)} + \delta \mathbf{r}_{j(t)}, \quad (13)$$

where $\mathbf{r}_{0,j} = (R_{ct}, \theta_{cj,t}, \phi_j)$ is obtained by optimization and $\mathbf{r}_{0,t} = (0, 0, 0)$. The displacements $\delta \mathbf{r}_{j(t)}$ originating from

the thermal motion of atoms, can be modeled as a 3D Gaussian function with widths $\sigma_{x,y,(z)} = \sqrt{k_B T_a / m w_{x,y,(z)}^2}$ for radial (axial) localizations. Inspired by the experimental data in Ref. [57] we consider two cases: $\sigma_x \in [0, 2.0] \mu\text{m}$, $\sigma_{y,z} = 0.27 \mu\text{m}$ and $\sigma_z \in [0, 2.0] \mu\text{m}$, $\sigma_{x,y} = 0.27 \mu\text{m}$. For Rb atoms held at a low temperature $T_a = 10 \mu\text{K}$, the optical trap with frequencies $2\pi \times 18.22$ and $2\pi \times 2.46$ kHz gives rise to position uncertainties of 0.27 and 2.0 μm , respectively. To estimate the errors from 3D position variations we also use the way of the stochastic Schrödinger equation [Eq. (8)] and obtain the numerical solution by averaging over 500 independent trajectories.

The numerical solutions in Figs. 3(a) and 3(c) indicate that the 3D gate protocol can show an unprecedented robustness to the fluctuated interactions in all directions. Because in a 3D optimal configuration the position variations of atoms can be partially overcome keeping the infidelity at a small level of 10^{-4} . In contrast, arranging (6+1) atoms in a 2D honeycomb lattice will lead to a clear enhancement of the infidelity as shown in Figs. 3(b) and 3(d). Particularly for the radial fluctuation the imperfection dramatically increases with σ_x , agreeing with previous results [57–59]. Note that a 1D chain model cannot preserve the asymmetric blockade condition so as to be unable to engineer a multiqubit quantum gate. Other technical imperfections such as the sensitivity to motional dephasing, laser intensity noise, and laser phase noise are discussed in Appendix F. A specific discussion for the

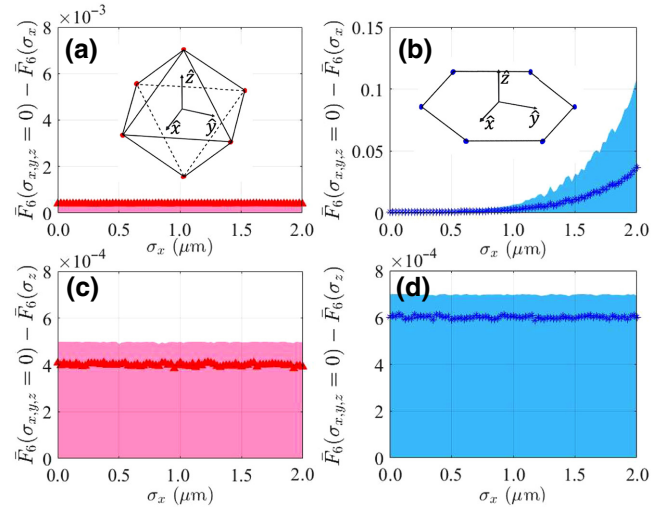


FIG. 3. Imperfection of the gate fidelity based on two different geometries versus the position variations along (a),(b) \hat{x} and (c),(d) \hat{z} directions. The standard deviations are $\sigma_{y,z} = 0.27 \mu\text{m}$ in (a),(b) and $\sigma_{x,y} = 0.27 \mu\text{m}$ in (c),(d). Each point denotes an average of 500 measurements. (a),(c)[or (b),(d)] are obtained from an optimal 3D C₆NOT gate [a 2D honeycomb-type (6+1) CNOT gate]. The shadings indicate a maximal position error during the calculation.

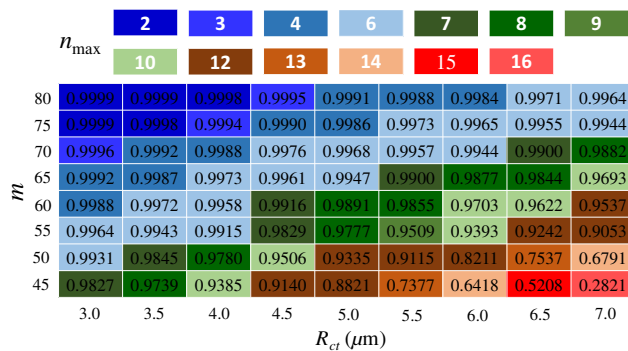


FIG. 4. Estimates of maximal control-atom number n_{\max} (top, color blocks) together with the average gate fidelity \bar{F}_n (black texts, estimated by $1 - \mathcal{E}_{n,se}$) in the space of (R_{ct}, m) . For different principal quantum number $m = (45, 50, 55, 60, 65, 70, 75, 80)$ and at a temperature of 77 K, the calculated coefficients are $C_6/2\pi = (-1, -2, -6, -12, -24, -57, -137, -288)$ GHz μm^6 , $C_3/2\pi = (1.370, 1.950, 2.912, 4.194, 5.859, 7.976, 10.620, 13.873)$ GHz μm^3 , the Rydberg decay rates are $\Gamma_s = (11.70, 8.55, 6.53, 5.00, 4.09, 3.33, 2.76, 2.33)$ kHz and $\Gamma_p = (6.85, 5.50, 4.26, 3.40, 2.73, 2.25, 1.88, 1.60)$ kHz. All parameters are taken from the ARC open-source library [44].

leakage error due to off-resonantly coupled Rydberg pair states, is given in Appendix B.

V. LARGE-SCALE MULTIQUBIT GATE

This multiqubit Toffoli gates can be treated as an alternative calculation unit for a large-scale quantum information processor [60]. Compared to traditional fewer-qubit gates [61–65] our protocol benefits from an optimal 3D geometry with arbitrary $n (< n_{\max})$ control atoms. To fully determine the maximal number n_{\max} we graphically study it by tuning the principal quantum number m and the spherical radius R_{ct} simultaneously. As shown in Fig. 4 it is clear that n_{\max} increases by lowering m since the asymmetry of interactions increases then, yet at the expense of the gate fidelity. Because the decay rates $\Gamma_{s(p)}$ grow at the same time, leading to a larger decay error. On the other hand, we find n_{\max} has a dramatic increase with the radius R_{ct} . Because for a same m the absolute values Ω_t and Ω_c , which depend on the control-target interaction U_{ct} [Eq. (11)], would strongly decrease if R_{ct} is enhanced. A smaller laser Rabi frequency will elongate the gate operation time, making the decay error dominant. So for $R_{ct} = 7 \mu\text{m}$ a C₁₂NOT gate suffers from a very low fidelity of 0.2821 when $m = 45$. A high-fidelity multicontrol Rydberg-blockade gate can be accomplished by a dual consideration of both the asymmetry and the Rydberg-state decay. Our theoretical estimation shows that a C₁₂NOT (12 control qubits and one target qubit) gate with a fidelity of 0.9537 is possible when $R_{ct} = 7 \mu\text{m}$ and $m = 60$.

VI. CONCLUSION AND OUTLOOK

We study a protocol of multicontrol-qubit Toffoli gates in which all control atoms are precisely arranged on a 3D spherical surface via optimization, which ensures the best asymmetric Rydberg blockade. These optimal geometries (see Fig. 1) are obtained by performing sufficient optimization based on evolutionary algorithm. Such a spheroidal gate has many advantages. First, it allows for a perfect preservation of strong Rydberg blockade between any control-target atom pairs, avoiding the effect of dramatic reduction in blockade strength due to distant control-target atoms as in 1D or 2D arrays. Second, an efficient optimization can ensure the best asymmetric Rydberg blockade leading to a negligible asymmetric blockade error. Finally, an unprecedented insensitivity approximately 10^{-4} to the position variations can be observed within the 3D gate due to the compensation of three-dimensional spacial fluctuations. In comparison, Ref. [57] reports a position error of 2.5×10^{-3} for a radius deviation of $0.16 \mu\text{m}$ via excitation annihilation mechanism. Our work shows a minimal error of 0.0463 when 12 control atoms monitor one target atom.

The scheme for an arbitrary $(n + 1)$ -qubit Toffoli gate can offer a direct route to multiqubit quantum computation. Upon the basis of one-step implementation to fewer-qubit quantum gates by our group recently [56], this 3D blockade-gate scheme can be used to reduce the number of fewer-qubit gates, greatly lowering the complexity of quantum device design [19,20]. Other straightforward applications with multiqubit gates refer to the production of Rydberg-mediated entanglement between two atom qubits [57] or within a mesoscopic ensemble of atoms [66], and of fast quantum computation with neutral Rydberg qubits [67].

ACKNOWLEDGMENTS

We acknowledge financial support from the Innovation Program for Quantum Science and Technology (Grant No. 2021ZD0303200), the National Key Research and Development Program of China (Grant No. 2016YFA0302001), the National Science Foundation of China (Grants No. 12174106, No. 12274376, No. 91950112, No. 11174081, No. 12234014, and No. 11654005), and the Shanghai Municipal Science and Technology Major Project (Grant No. 2019SHZDZX01), the Science and Technology Commission of Shanghai Municipality (Grant No. 18ZR1412800), and the ECNU Academic Innovation Promotion Program for Excellent Doctoral Students (Grant No. YBNLTS2019-023). W.Z. also acknowledges additional support from the Shanghai talent program.

APPENDIX A: ASYMMETRIC INTERACTIONS

Taking account of the scheme feasibility we present details on the Rydberg pair states and their interactions

in order to show the establishment of asymmetric interactions. We assume the two Rydberg states of each atom, which are $|s_{l,j}\rangle = |61S_{1/2}, 1/2\rangle$, $|p_{l,j}\rangle = |60P_{3/2}, 3/2\rangle$. In the presence of a static electric field, when two atoms (control and target) are prepared in two different dipole-coupled Rydberg states such as $|p_j\rangle$ and $|s_t\rangle$, the pair state $|p_j s_t\rangle$ is directly coupled to the same-energy state $|s_j p_t\rangle$ by a resonant dipole-dipole exchange interaction. Typically this dipole-dipole interaction \mathcal{B} between a pair of Rydberg atoms can be given by [68]

$$\mathcal{B} = \frac{1}{4\pi\epsilon_0} \left[\frac{\boldsymbol{\mu}_1 \cdot \boldsymbol{\mu}_2}{R^3} - 3 \frac{(\boldsymbol{\mu}_1 \cdot \mathbf{R})(\boldsymbol{\mu}_2 \cdot \mathbf{R})}{R^5} \right], \quad (\text{A1})$$

where $\boldsymbol{\mu}_{1,2}$ stands for the electric dipole transition operators and ϵ_0 the permittivity of a vacuum. \mathbf{R} is the internuclear distance and $R = |\mathbf{R}|$. Moreover an external static electric field \vec{E} defines the quantization axis \hat{z} , which controls the orientation of the dipole moments relative to the separation vector \mathbf{R} , yielding an anisotropic dipole-dipole interaction,

$$\begin{aligned} \mathcal{B}(\theta_{c_j t}) = & \\ & \frac{1}{4\pi\epsilon_0 R^3} \{ \mu_{1+} \mu_{2-} + \mu_{1-} \mu_{2+} + \mu_{1z} \mu_{2z} (1 - 3 \cos^2 \theta_{c_j t}) \\ & - \frac{3 \sin^2 \theta_{c_j t}}{2} (\mu_{1+} \mu_{2+} + \mu_{1+} \mu_{2-} + \mu_{1-} \mu_{2+} + \mu_{1-} \mu_{2-}) \\ & - \frac{3 \sin \theta_{c_j t} \cos \theta_{c_j t}}{\sqrt{2}} (\mu_{1+} \mu_{2z} + \mu_{1-} \mu_{2z} \\ & + \mu_{1z} \mu_{2+} + \mu_{1z} \mu_{2-}) \}. \end{aligned} \quad (\text{A2})$$

with $\theta_{c_j t}$ the polarizing angle between the internuclear axis and the quantization axis \hat{z} . $\mu_{v,(x,y,z)}$ denotes the projections of dipole matrix element $\boldsymbol{\mu}_v$ onto axis $\hat{x}, \hat{y}, \hat{z}$ and $\mu_{v,\pm} = \mu_{v,x} \pm i\mu_{v,y}$ with $v \in (1, 2)$. Accounting for the use of σ -polarized transition between $|60P_{3/2}, m_j = 3/2\rangle$ and $|61S_{1/2}, m_j = 1/2\rangle$ with respect to $\Delta m_j = \pm 1$, we can ignore the term $\mu_{1z} \mu_{2z}$, which requires $\Delta m_j = 0$. Then Eq. (A2) can be reorganized as

$$\begin{aligned} \mathcal{B}(\theta_{c_j t}) &= - \frac{(1 - 3 \cos^2 \theta_{c_j t})}{8\pi\epsilon_0 R^3} (\mu_{1+} \mu_{2-} + \mu_{1-} \mu_{2+}) \\ & - \frac{3 \sin^2 \theta_{c_j t}}{8\pi\epsilon_0 R^3} [\mu_{1+} \mu_{2+} + \mu_{1-} \mu_{2-} \\ & + \frac{\sqrt{2} \cos \theta_{c_j t}}{\sin \theta_{c_j t}} (\mu_{1+} \mu_{2z} + \mu_{1-} \mu_{2z} \\ & + \mu_{1z} \mu_{2+} + \mu_{1z} \mu_{2-})]. \end{aligned} \quad (\text{A3})$$

Apparently, there are three types of angular dependence in Eq. (A3) while only the first term $\propto (1 - 3 \cos^2 \theta_{c_j t})$

is appropriate. This corresponds to a resonant exchange energy between states $|s_j p_t\rangle \xleftrightarrow{\omega} |p_j s_t\rangle$ where $\Delta m_j = +1$ for one atom and $\Delta m_j = -1$ for the other. Other possible transitions connecting with same combinations of $\Delta m_j = \pm 1$, are off-resonantly coupled due to a big Stark shift via the electric field [68]. An estimation of the leakage error to the gate fidelity from these nonresonant Rydberg levels is illustrated in Appendix B.

In the main text we expect a resonant dipole-dipole interaction strength that varies only as

$$\langle s_{j(t)} p_{t(j)} | \mathcal{B}(\theta_{c_j t}) | p_{j(t)} s_{t(j)} \rangle = \frac{C_3^{sp}(\theta_{c_j t})}{R_{ct}^3}, \quad (\text{A4})$$

where $R_{ct} = R$ means the two-atom separation and the interaction coefficient C_3^{sp} scaling as m^4 takes a complex form of

$$C_3^{sp}(\theta_{c_j t}) = \frac{|\mu_{sp}|^2 (1 - 3 \cos^2 \theta_{c_j t})}{8\pi\epsilon_0}, \quad (\text{A5})$$

and the transition matrix element is

$$\mu_{sp} = \langle 61S_{1/2}, m_j = 1/2 | \mu | 60P_{3/2}, m_j = 3/2 \rangle.$$

Finally, we can obtain the electric dipole-dipole Hamiltonian between a pair of control and target atoms, which is

$$\hat{U}_{c_j t}^{sp}(\theta_{c_j t}) = \frac{C_3^{sp}(\theta_{c_j t})}{R_{ct}^3} (|p_j s_t\rangle \langle s_j p_t| + |s_j p_t\rangle \langle p_j s_t|). \quad (\text{A6})$$

On the other hand, as for two control atoms, which are prepared in the same Rydberg level such as $|60P_{3/2}, m_j = 3/2\rangle$ the electric dipole-dipole interaction \mathcal{B} plays only roles at the second order in perturbation theory since an atomic state has a vanishing average electric dipole moment to the first order of perturbation [69]. As a result via \mathcal{B} the pair state $|p_j p_{j'}\rangle = |60P_{3/2}, 60P_{3/2}\rangle$ is coupled to other nearby pair states of opposite parity where the energy of those states differs from that of $|60P_{3/2}, 60P_{3/2}\rangle$ by a big quantity. The average effect gives rise to a second-order vdW shift of the considered pair state $|p_j p_{j'}\rangle$ scaling as $\propto C_6 / R_{c_j c_{j'}}^6$ where the coefficient C_6 roughly scales as m^{11} (m is the principal quantum number). Details about the influence from original nonresonant dipole-dipole coupled states are discussed in Appendix B. Therefore, the reduced vdW-type interaction Hamiltonian can be described by

$$\hat{U}_{c_j c_{j'}} = \frac{C_6}{R_{c_j c_{j'}}^6} |p_j p_{j'}\rangle \langle p_j p_{j'}|. \quad (\text{A7})$$

From Eqs. (A6) and (A7) it is apparent that both the dipole-dipole and vdW interactions between two Rydberg

atoms depend on the interatomic separation. To reach a huge asymmetry in the interaction, i.e., $(C_3^{sp}(\theta_{c_j t})/R_{ct}^3 \gg C_6/(R_{c_j c_j'}^6))$, we have to seek for optimal distributions of all control atoms on the spherical surface, see more details in Sec. II.

APPENDIX B: LEAKAGE ERROR ESTIMATION

Leakage error based on two-atom states. As illustrated in Fig. 5(a) we consider a resonant dipole-dipole interaction between one control atom and one target atom for the $|p_j s_t\rangle \rightleftharpoons |s_j p_t\rangle$ transition. In a real implementation these two-atom pair states might still experience nonresonant dipole-dipole couplings to other undesired Rydberg pair states, resulting in a leakage error to the gate fidelity. Here the nonresonant coupling strength and the Förster energy defect are denoted as B_κ and δ_κ , respectively. Our task is to find out the influence of these nonresonant couplings to the gate fidelity estimated in our protocol. In principle we should sum over all selection-rule permitted transitions over a wide range of principal quantum numbers and calculate the leakage error. Here we check all possible transitions from $|p_j s_t\rangle$ and $|s_j p_t\rangle$ to other leakage states and find that the influence of a farther state can be almost negligible due to its weaker coupling strength B_κ or a larger energy defect δ_κ . In the calculation the factor B_κ/δ_κ is used

to characterize the leakage strength that is proportional to the leakage error. If $B_\kappa/\delta_\kappa \ll 1$ the leakage from the resonantly coupled state can be suppressed [63].

In Fig. 5(a) and Table I(left) we show the possible transitions with the change of principal quantum number up to ± 2 from the resonant pair states $|p_j s_t\rangle \rightleftharpoons |s_j p_t\rangle$. To estimate the gate error due to the leakage of population from these states, we solve the stochastic Schrödinger equation (8) with respect to the Hamiltonian

$$\begin{aligned} \mathcal{H}_{ps} = & \frac{1}{2}\Omega_2(t)|p_j 1_t\rangle\langle p_j s_t| + \frac{1}{2}\Omega_3(t)|p_j s_t\rangle\langle p_j 0_t| \\ & + (B_0|p_j s_t\rangle\langle s_j p_t| + B_\kappa|p_j s_t\rangle\langle a_{\kappa j} b_{\kappa t}| \\ & + B_\kappa|s_j p_t\rangle\langle b_{\kappa j} a_{\kappa t}| \\ & + \text{H.c.}) + \delta_\kappa(|b_{\kappa j} a_{\kappa t}\rangle\langle b_{\kappa j} a_{\kappa t}| + |a_{\kappa j} b_{\kappa t}\rangle\langle a_{\kappa j} b_{\kappa t}|), \end{aligned} \quad (B1)$$

where we treat $|p_j 1_t\rangle$ as the initial state and apply two pulses $\Omega_2(t)$ and $\Omega_3(t)$. Ideally a preexcitation of the control atom would block the excitation of the target atom so the population missing from state $|p_j 1_t\rangle$ can be regarded as the leakage error. See the last column of Table I(left), the population rotation error shows a clear decrease from case 1 to case 4 and it is almost negligible in cases 3 and 4 due to the tiny leakage error in the range of 10^{-7} – 10^{-5} . Based on the results we choose two pairs of nonresonant

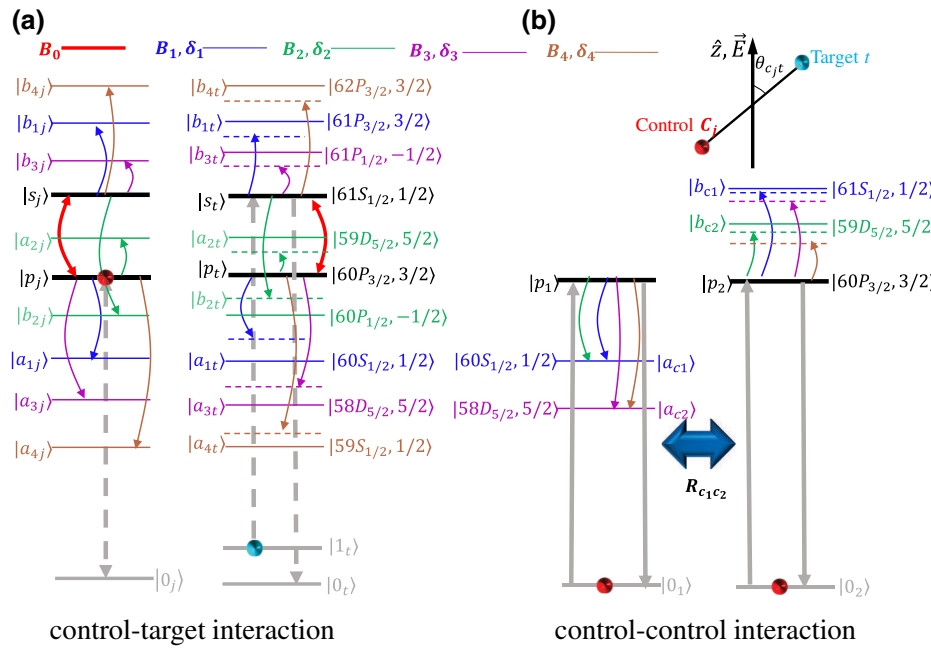


FIG. 5. (a) For one control and one target atom, some dominant leakage levels with respect to the resonant dipole-dipole interaction between $|p_j s_t\rangle$ and $|s_j p_t\rangle$, where $|p_{j,t}\rangle = |60P_{3/2}, 3/2\rangle$ and $|s_{j,t}\rangle = |61S_{1/2}, 1/2\rangle$. Other selection-rule permitted pair states are off-resonantly coupled by obeying $|p_j s_t\rangle \rightleftharpoons |a_{\kappa j} b_{\kappa t}\rangle$ (forward) and $|s_j p_t\rangle \rightleftharpoons |b_{\kappa j} a_{\kappa t}\rangle$ (backward) with strength B_κ and Förster energy defect δ_κ and $\kappa \in (1, 2, 3, 4)$. (b) Some leakage levels related to the detuned dipole-dipole interaction between two control atoms where $|p_1 p_2\rangle = |60P_{3/2}, 3/2; 60P_{3/2}, 3/2\rangle$. B_κ and δ_κ represent the coupling strength and the corresponding energy defect between $|p_1 p_2\rangle$ and other undesired nonresonant Rydberg pair states $|Pr_\kappa\rangle = \{|a_{c1} b_{c1}\rangle, |a_{c1} b_{c2}\rangle, |a_{c2} b_{c1}\rangle, |a_{c2} b_{c2}\rangle\}$, where $|a_{c1}\rangle = |60S_{1/2}, 1/2\rangle$, $|a_{c2}\rangle = |58D_{5/2}, 5/2\rangle$, $|b_{c1}\rangle = |61S_{1/2}, 1/2\rangle$, $|b_{c2}\rangle = |59D_{5/2}, 5/2\rangle$.

TABLE I. Leakage error due to the presence of several nonresonant dipole-dipole coupled states nearby. Table(left): leakage states for the resonant pair states $|p_j s_t\rangle$ and $|s_j p_t\rangle$, which are $|p_j s_t\rangle \rightleftharpoons |a_{kj} b_{\kappa t}\rangle$ (forward) and $|s_j p_t\rangle \rightleftharpoons |b_{kj} a_{\kappa t}\rangle$ (backward) with strength $B_\kappa = C_3^{sp(\kappa)} / R_{ct}^3 (C_3^{sp(\kappa)})$ is in units of $2\pi \times \text{GHz } \mu\text{m}^3$) and energy defect $\delta_\kappa / 2\pi = (0.8771, 7.8032, 8.6142, 5.3452)$ GHz. Here $\theta_{c_j t} = 0$ and $B_0 = C_3^{sp}(0) / R_{ct}^3$ with $C_3^{sp}(0) / 2\pi = -8.388$ GHz μm^3 . $R_{ct} = 5 \mu\text{m}$ treats as the radius of sphere and the leakage error $1 - P_{p_j 1_t}$ is estimated by calculating the population missing from state $|p_j 1_t\rangle$. Table(right): off-resonance pair states $|Pr_\kappa\rangle$ with respect to $|p_1 p_2\rangle$, i.e., $|p_1 p_2\rangle \rightleftharpoons |Pr_\kappa\rangle$ enabled by a nonresonant dipole-dipole interaction $B_\kappa = C_3^{(\kappa)} / R_{c_1 c_2}^3 (C_3^{(\kappa)})$ is in unit of $2\pi \times \text{GHz } \mu\text{m}^3$). Here the energy defect is $\delta_\kappa / 2\pi = (0.2784, 7.0614, 7.4587, 14.8012)$ GHz and $\epsilon_{1,2}$ stand for the leakage error from state $|0_1 0_2\rangle$ under different interatomic distances $R_{c_1 c_2} = (2R_{ct}, R_{ct}) \mu\text{m}$. All parameters are taken from the ARC open-source library [44].

κ	$ a_{kj}\rangle = a_{\kappa t}\rangle$	$ b_{kj}\rangle = b_{\kappa t}\rangle$	$C_3^{sp(\kappa)}(0)$	B_κ / δ_κ	$1 - P_{p_j 1_t}$	$ Pr_\kappa\rangle$	$C_3^{(\kappa)}$	ϵ_1	ϵ_2
1	$ 60S_{1/2}, \frac{1}{2}\rangle$	$ 61P_{3/2}, \frac{3}{2}\rangle$	-9.134	8.3×10^{-2}	9.11×10^{-4}	$ 60S_{1/2}, \frac{1}{2}; 61S_{1/2}, \frac{1}{2}\rangle$	4.301	4.27×10^{-5}	3.21×10^{-2}
2	$ 59D_{5/2}, \frac{5}{2}\rangle$	$ 60P_{1/2}, -\frac{1}{2}\rangle$	-9.254	9.5×10^{-3}	1.32×10^{-4}	$ 60S_{1/2}, \frac{1}{2}; 59D_{5/2}, \frac{5}{2}\rangle$	5.919	2.69×10^{-8}	8.09×10^{-6}
3	$ 58D_{5/2}, \frac{5}{2}\rangle$	$ 61P_{3/2}, -\frac{1}{2}\rangle$	-3.926	3.6×10^{-3}	3.93×10^{-5}	$ 58D_{5/2}, \frac{5}{2}; 61S_{1/2}, \frac{1}{2}\rangle$	3.203	2.15×10^{-8}	8.76×10^{-6}
4	$ 59S_{1/2}, \frac{1}{2}\rangle$	$ 62P_{3/2}, \frac{3}{2}\rangle$	-0.14	2.1×10^{-4}	3.57×10^{-7}	$ 58D_{5/2}, \frac{5}{2}; 59D_{5/2}, \frac{5}{2}\rangle$	4.408	1.43×10^{-8}	8.75×10^{-6}

coupled states: $|a_{1j} b_{1t}\rangle$ and $|b_{1j} a_{1t}\rangle (\kappa = 1)$, $|a_{2j} b_{2t}\rangle$ and $|b_{2j} a_{2t}\rangle (\kappa = 2)$ as the dominant leakage states with respect to the resonant transition between $|p_j s_t\rangle \rightleftharpoons |s_j p_t\rangle$.

In addition we study the leakage error due to the nonresonant dipole-dipole couplings with respect to the identical Rydberg pair state $|p_1 p_2\rangle$ for two control atoms. Here we apply four pairs of dipole-allowed off-resonantly coupled states $|Pr_\kappa\rangle$ with strength $B_\kappa = C_3^{(\kappa)} / R_{c_1 c_2}^3$ and Förster energy defect δ_κ , see Table I(right). In principle we have to sum up all possible nonresonant states at the same time, which leads to a second-order level shift of $|p_1 p_2\rangle$ represented by a coefficient $C_6 \approx \sum_\kappa (C_3^{(\kappa)})^2 / \delta_\kappa$.

In the calculation we again calculate the dynamics of a two-atom state $|0_1 0_2\rangle$ by following the Hamiltonian of

$$\mathcal{H}_{pp} = \sum_j^2 \mathcal{H}_j + (B_\kappa |p_1 p_2\rangle \langle Pr_\kappa| + H.c.) + \delta_\kappa |Pr_\kappa\rangle \langle Pr_\kappa| \quad (B2)$$

where $\mathcal{H}_j = 1/2(\Omega_1(t)|p_j\rangle \langle 0_j| + \Omega_5(t)|0_j\rangle \langle p_j|)$. Starting from the initial state $|0_1 0_2\rangle$ we numerically estimate the population missing from $|0_1 0_2\rangle (\epsilon_{1(2)} = 1 - P_{0_1 0_2})$ by applying two separated π pulses $\Omega_1(t)$ and $\Omega_5(t)$. Note that the nonresonant coupling strength B_κ is inversely proportional to the interatomic distance $R_{c_1 c_2}$ so we use different values $R_{c_1 c_2} = (2R_{ct}, R_{ct}) \mu\text{m}$. See the last two columns in Table I, for a larger distance the leakage error ϵ_1 is always below 10^{-4} in all cases, which means these off-resonantly coupled levels play a negligible effect and it is reasonable to assume a pure vdW shift represented by $C_6 / R_{c_1 c_2}^6$ for the $|p_1 p_2\rangle$ state. However, if the two-atom distance is too small, e.g., $R_{c_1 c_2} = R_{ct}$, it is inappropriate to assume a vdW interaction because the pair state $|Pr_1\rangle$ can cause a big leakage error approximately 0.0321, which is even larger than the intrinsic decay error. In all cases we find the effect of other nonresonant states $|Pr_{2-4}\rangle$ can be ignored as compared with $|Pr_1\rangle$. Based on the analysis above we treat $|Pr_1\rangle$ as the dominant leakage state with respect to

$|p_1 p_2\rangle$ and will include it in evaluating the leakage error of a realistic multiqubit quantum gate.

Leakage error based on a multiqubit quantum gate. To correctly show the results reasonable in the main text, we now discuss the real implementation of a multiqubit quantum gate by taking account of off-resonant dipole-dipole couplings from dominant leakage states. The system we simulate consists of n control atoms and one target atom described by the Hamiltonian of

$$\hat{\mathcal{H}} = \hat{\mathcal{H}}_0 + \hat{\mathcal{H}}_I. \quad (B3)$$

Here the first term $\hat{\mathcal{H}}_0$ as shown in Eq. (5) describes the resonant atom-light couplings of control and target atoms. The second term $\hat{\mathcal{H}}_I$ [see Eq. (6)] describes the Rydberg states and their interactions, where the resonant dipole-dipole interaction for control-target atom pairs is (here $\kappa = 1, 2$)

$$\begin{aligned} \hat{U}_{c_j t} = & (B_0 |p_j s_t\rangle \langle s_j p_t| + B_\kappa |p_j s_t\rangle \langle a_{kj} b_{\kappa t}| \\ & + B_\kappa |s_j p_t\rangle \langle b_{kj} a_{\kappa t}| + H.c.) + \delta_\kappa (|b_{kj} a_{\kappa t}\rangle \langle b_{kj} a_{\kappa t}| \\ & + |a_{kj} b_{\kappa t}\rangle \langle a_{kj} b_{\kappa t}|), \end{aligned} \quad (B4)$$

and the nonresonant dipole-dipole interaction between two identical control atoms takes the form of (here $\kappa = 1$)

$$\hat{U}_{c_j c_j} = (B_\kappa |p_1 p_2\rangle \langle Pr_\kappa| + H.c.) + \delta_\kappa |Pr_\kappa\rangle \langle Pr_\kappa|, \quad (B5)$$

with the strength B_κ and the Förster energy defect δ_κ estimated in Table I. Note that the coefficient $C_3^{sp(\kappa)}$ depends on a varying polarizing angle $\theta_{c_j t}$ while in Table I we set $\theta_{c_j t} = 0$.

In the numerical simulation we first consider $n = 2$, which is a three-qubit Toffoli gate showing a linear structure in space. We calculate the average gate fidelity $\bar{\mathcal{F}}_2$ [see Eq. (7)] over eight input states $|\Psi_{in}\rangle = \{|000\rangle, |001\rangle, |010\rangle, |011\rangle, |100\rangle, |101\rangle, |110\rangle, |111\rangle\}$ by

evolving the stochastic Schrödinger equation. The output state $|\bar{\Psi}_{\text{out}}\rangle$ is obtained at $t = t_{\text{det}}$ after 500 stochastic evolutions. Via taking account of the dominant leakage states we finally find the average gate fidelity is $\bar{\mathcal{F}}_2 = 0.997\ 937\ 41$. As compared with $\bar{\mathcal{F}}_2 = 0.998\ 323\ 54$ obtained in the case of no nonresonant states, this value is slightly decreased by 3.9×10^{-4} . The small leakage error caused by nonresonant couplings, means that the asymmetric blockade interactions can be well preserved in the implementation of a $(2 + 1)$ -qubit gate.

More remarkably, we also calculate a realistic spheroidal quantum gate with four control atoms and one target atom since different atomic distances and polarizing angles must be affected. After a computer-demanding calculation we finally obtain $\bar{\mathcal{F}}_4 = 0.993\ 602\ 69$, which leads to a leakage error of 7.1×10^{-4} with respect to the case that ignores the nonresonant couplings. In Fig. 2 we show that the average gate fidelity for the case of $n = 4$ is $0.994\ 315\ 26$. This slight growth of the leakage error with the number of control atoms mainly comes from a slightly weaker asymmetry in the interaction. Because as n increases, the nonresonant coupling strength, which depends on the interatomic distance $R_{c_j c_j'}$, becomes stronger giving rise to a bigger leakage. However our simulations confirm that, by considering off-resonantly coupled Rydberg states the leakage error for a realistic 3D multiqubit quantum gate can still be kept at a negligible level approximately 10^{-4} . Therefore the 3D multiqubit gate presented in the main text can be implemented in a realistic environment, which is enabled by a large symmetry in the interaction.

APPENDIX C: EVOLUTIONARY ALGORITHM

In this section we demonstrate how to get optimal geometries of control atoms on the surface and determine the value n_{\max} via evolutionary algorithm. Taking C₆NOT gate as an example, first we randomly arrange the initial positions of control atoms c_j denoted as $\mathbf{r}_j^{(0)} = (R_{ct}, \theta_j^{(0)}, \phi_j^{(0)})$ where the superscript “0” means the initial step $p = 0$. For a finite spherical radius R_{ct} , one has $\mathbf{r}_j^{(0)} = (\theta_j^{(0)}, \phi_j^{(0)})$ and $j \in [1, 6]$. Then we compare all asymmetry factors $\chi_j^{(0)} = U_{cj,t}/U_{c_j c_j'}$, with respect to atom c_j where the total number is $c_6^2 = 15$, in order to find a minimal value

$$\chi_0 = \min(\chi_j^{(0)}). \quad (\text{C1})$$

Next we add a small perturbation to the position of control atoms, leading to

$$\mathbf{r}_j^{(1)} = (\theta_j^{(0)} + \delta\theta_j, \phi_j^{(0)} + \delta\phi_j), \quad (\text{C2})$$

in which $\delta\theta_j$ or $\delta\phi_j$ is obtained randomly from the range of $[-0.1\theta_j^{(0)}, 0.1\theta_j^{(0)}]$ or $[-0.1\phi_j^{(0)}, 0.1\phi_j^{(0)}]$. With the alternative position $\mathbf{r}_j^{(1)}$ we again compare all $\chi_j^{(1)}$ values and

find out a minimal value, which is denoted as $\min(\chi_j^{(1)})$. To maximize asymmetric blockade, χ_1 is defined as

$$\chi_1 = \max(\min(\chi_j^{(0)}), \min(\chi_j^{(1)})), \quad (\text{C3})$$

at step $p = 1$ and the corresponding position $\mathbf{r}_j^{(0)}$ or $\mathbf{r}_j^{(1)}$ will be ready for the next-step ($p = 2$) optimization. This single-optimization process must be repeated with sufficient iterations (typically $p > 10^5$) until the condition $|\chi_p - \chi_{p-1}| < 10^{-5}$ is met where the universal maximal asymmetry factor is given by

$$\chi_p = \max(\min(\chi_j^{(0)}), \min(\chi_j^{(1)}), \dots, \min(\chi_j^{(p)})). \quad (\text{C4})$$

In order to avoid a local optimal solution we perform 10^4 optimization runs via evolutionary algorithm and achieve the optimal distribution of control atoms $\mathbf{r}_j = (\theta_j, \phi_j)$. As shown in Fig. 1(a) the position of c_2 is obtained after 10^4 optimizations, which are very condensed in space. To quantitatively verify this effect, in Table II(i)–(v) we exemplify five sets of parameters to show the robustness of our optimization algorithm. Given the initial positions $(\theta_j^{(0)}, \phi_j^{(0)})$ [first row of (i)–(v)], the results from single optimization [second row of (i)–(v)] are very close to the average results after taking 10^4 optimizations, which confirms the accuracy of evolutionary algorithm. For ensuring a huge asymmetry we also set a limitation $\chi_p > 100$ in the optimization, which gives rise to a maximal n_{\max} permitted if m and R_{ct} are determined. For example, in the case of $m = 60$ and $R_{ct} = 5 \mu\text{m}$, $n = 8$ leads to $\chi_p = 102.986$, while $n = 9$ leads to $\chi_p = 64.310$, which breaks the limitation, so $n_{\max} = 8$ is obtained.

APPENDIX D: OPTIMAL GEOMETRY

Case of two control atoms. To provide a physical understanding for these optimal configurations we study the potentials of the system. The basic ingredient in optimization is to maximize the asymmetry of interaction, arising $U_{cj,t} \gg U_{c_j c_j'}$. To achieve this, we explore the essential feature of the system by concentrating on the Rydberg states $|p_{j,t}\rangle, |s_{j,t}\rangle$, which connect with the interaction Hamiltonians, Eqs. (1)–(2). Here the index $j = 1, \dots, n$ represents the number of control atoms, and t labels the target atom. We analyze the interaction potential in the subspace only involving Rydberg states spanned by collective states $|\pi_i\rangle (i = 1, \dots, n)$, which means i control atoms are in $|p\rangle$ and others are in $|s\rangle$ [70]. For $n = 2$, states $|\pi_i\rangle$ can be written as

$$|\pi_1\rangle = \frac{1}{\sqrt{2}}(|s_1 p_2 p_t\rangle + |p_1 s_2 p_t\rangle), \quad (\text{D1})$$

$$|\pi_2\rangle = |p_1 p_2 s_t\rangle.$$

Due to the exchange property of resonant dipole-dipole interaction $|p_j s_t\rangle \rightleftharpoons |s_j p_t\rangle$ this complete set of

TABLE II. (i)–(v) Five sets of parameters for random initialization $(\theta_j^{(0)}, \phi_j^{(0)})$ of atomic positions (first row) and for optimized positions $[(\theta_j, \phi_j)]$, second row] under one optimization run. Average results (last row) indicates datum averaging over 10^4 optimizations.

Case	c_1	c_2	c_3	c_4	c_5	c_6
(i)	$(\pi/2, \pi/6)$ (1.5731, 3.1421)	$(\pi/2, \pi/2)$ (1.5747, 4.7111)	$(\pi/2, 5\pi/6)$ (1.5732, 0)	$(\pi/2, 7\pi/6)$ (1.5705, 1.5694)	$(\pi/2, 3\pi/2)$ (0.0027, 0.0007)	$(\pi/2, 11\pi/6)$ (3.1412, 0.0012)
(ii)	$(0, 0)$ (1.5743, 3.1433)	$(\pi/5, 2\pi/5)$ (1.5744, 4.7136)	$(2\pi/5, 4\pi/5)$ (1.5722, 0)	$(3\pi/5, 6\pi/5)$ (1.5724, 1.5753)	$(4\pi/5, 8\pi/5)$ (0.0003, 0.0008)	$(\pi, 2\pi)$ (3.1408, 0.0056)
(iii)	$(\pi/6, \pi/5)$ (1.5701, 3.1403)	$(\pi/3, 2\pi/5)$ (1.5697, 4.7125)	$(\pi/2, 3\pi/5)$ (1.5711, 0)	$(2\pi/3, 4\pi/5)$ (1.5707, 1.5731)	$(5\pi/6, \pi)$ (0.0010, 0.0011)	$(\pi, 6\pi/5)$ (3.1419, 0.0023)
(iv)	$(\pi/7, \pi/5)$ (1.5705, 3.1419)	$(2\pi/7, \pi/6)$ (1.5711, 4.7119)	$(3\pi/7, \pi/7)$ (1.5695, 0)	$(4\pi/7, \pi/8)$ (1.5703, 1.5718)	$(5\pi/7, \pi/9)$ (0.0002, 0.0005)	$(6\pi/7, \pi/10)$ (3.1416, 0.0003)
(v)	$(\pi/8, \pi)$ (1.5713, 3.1408)	$(\pi/4, \pi/2)$ (1.5716, 4.7119)	$(3\pi/8, \pi/3)$ (1.5701, 0)	$(\pi/2, \pi/4)$ (1.5695, 1.5705)	$(5\pi/8, \pi/5)$ (0.0013, 0.0007)	$(3\pi/4, \pi/6)$ (3.1415, 0.0001)
Average results	(1.5708, 3.1416)	(1.5707, 4.7124)	(1.5709, 0)	(1.5708, 1.5707)	(0.0005, 0.0006)	(3.1416, 0.0007)

basis is equivalent to the form of $\{|\pi_0\rangle, |\pi_1\rangle\} = \{|s_1 s_1 p_t\rangle, 1/\sqrt{2}(|s_1 p_2 s_t\rangle + |p_1 s_2 s_t\rangle)\}$. In the basis of $|\pi_1\rangle$ and $|\pi_2\rangle$ as in Eq. (D1), the effective interaction Hamiltonian $\mathcal{H}_{n,\text{int}}$ is given by ($n = 2$)

$$\mathcal{H}_{2,\text{int}} = \begin{pmatrix} 0 & \frac{1}{\sqrt{2}} D_2 \\ \frac{1}{\sqrt{2}} D_2 & B_2 \end{pmatrix}, \quad (\text{D2})$$

where $D_n = \sum_{j=1}^n U_{c_j t}$ and $B_n = \sum_{j>j'} U_{c_j c_{j'}}$, and $j, j' \in [1, \dots, n]$. Analytical diagonalization of the Hamiltonian matrix yields the eigenenergies, explicitly as

$$E_{\pm} = \frac{B_2 \pm \sqrt{B_2^2 + 2D_2^2}}{2}. \quad (\text{D3})$$

It is apparent that, in Eq. (D2) the off-diagonal resonant dipole-dipole interaction $U_{c_j t}(\theta_{c_j t}) \propto (1 - 3 \cos^2(\theta_{c_j t}))$ is responsible for the population transfer between different $|\pi_i\rangle$ states, which leads to anisotropic spatial interactions. The diagonal term $U_{c_1 c_2} \propto |\mathbf{r}_{c_1} - \mathbf{r}_{c_2}|^{-6}$ also depends on the relative distance between two control atoms c_1 and c_2 . We restrict all control atoms on the spherical surface so $U_{c_1 c_2}$ is minimized when two atoms are separated by a maximal distance which is $2R_{ct}$ (diameter), leading to $\theta = \theta_{c_1 t} = \pi - \theta_{c_2 t}$. In this case D_2 and B_2 take explicit expressions as

$$D_2 = \frac{2C_3(1 - 3 \cos^2 \theta)}{R_{ct}^3}, B_2 = \frac{C_6}{(2R_{ct})^6}, \quad (\text{D4})$$

and the eigenenergies of two collective states $|\pi_{1,2}\rangle$ can be independently controlled by a single polarizing angle θ .

As shown in Fig. 6(a), we show the eigenenergies E_{\pm} as a function of the polarizing angle θ . For $\theta = 0$ or π the minimum of potential occurs, which means the attractive dipole-dipole interaction D_2 attains its maximal (absolute) magnitude. In other words when the two control atoms are

placed at $(\theta, \phi) = (0, 0)$ and $(\pi, 0)$ the asymmetric interaction could be maximized (note that B_2 is a constant). Our result based on numerical optimization also gives the same structure as the theoretical prediction, see Fig. 1 ($n = 2$). To this end we confirm the accuracy of the evolutionary algorithm, which helps to obtain a maximal asymmetric interaction by positioning atoms appropriately on the spherical surface.

Case of four control atoms. The situation becomes quite complex when more control atoms are included, because the magnitude of potential energy is influenced by multiple adjustable parameters. As examples we analyze the case of $n = 4$. With the inclusion of more Rydberg states the collective $|\pi_i\rangle$ states can be rewritten as

$$\begin{aligned} |\pi_1\rangle &= \frac{1}{2}(|p_1 s_2 s_3 s_4 p_t\rangle + |s_1 p_2 s_3 s_4 p_t\rangle + |s_1 s_2 p_3 s_4 p_t\rangle \\ &\quad + |s_1 s_2 s_3 p_4 p_t\rangle), \\ |\pi_2\rangle &= \frac{1}{\sqrt{6}}(|p_1 p_2 s_3 s_4 s_t\rangle + |p_1 s_2 p_3 s_4 s_t\rangle + |p_1 s_2 s_3 p_4 s_t\rangle \\ &\quad + |s_1 p_2 p_3 s_4 s_t\rangle + |s_1 p_2 s_3 p_4 s_t\rangle + |s_1 s_2 p_3 p_4 s_t\rangle), \\ |\pi_3\rangle &= \frac{1}{2}(|p_1 p_2 p_3 s_4 p_t\rangle + |p_1 p_2 s_3 p_4 p_t\rangle + |p_1 s_2 p_3 p_4 p_t\rangle \\ &\quad + |s_1 p_2 p_3 p_4 p_t\rangle), \\ |\pi_4\rangle &= |p_1 p_2 p_3 p_4 s_t\rangle, \end{aligned} \quad (\text{D5})$$

giving rise to the effective interaction Hamiltonian $\mathcal{H}_{4,\text{int}}$ given by

$$\mathcal{H}_{4,\text{int}} = \begin{pmatrix} 0 & \frac{\sqrt{3}}{2\sqrt{2}} D_4 & 0 & 0 \\ \frac{\sqrt{3}}{2\sqrt{2}} D_4 & \frac{1}{6} B_4 & 0 & 0 \\ 0 & 0 & \frac{1}{2} B_4 & \frac{1}{2} D_4 \\ 0 & 0 & \frac{1}{2} D_4 & B_4 \end{pmatrix}, \quad (\text{D6})$$

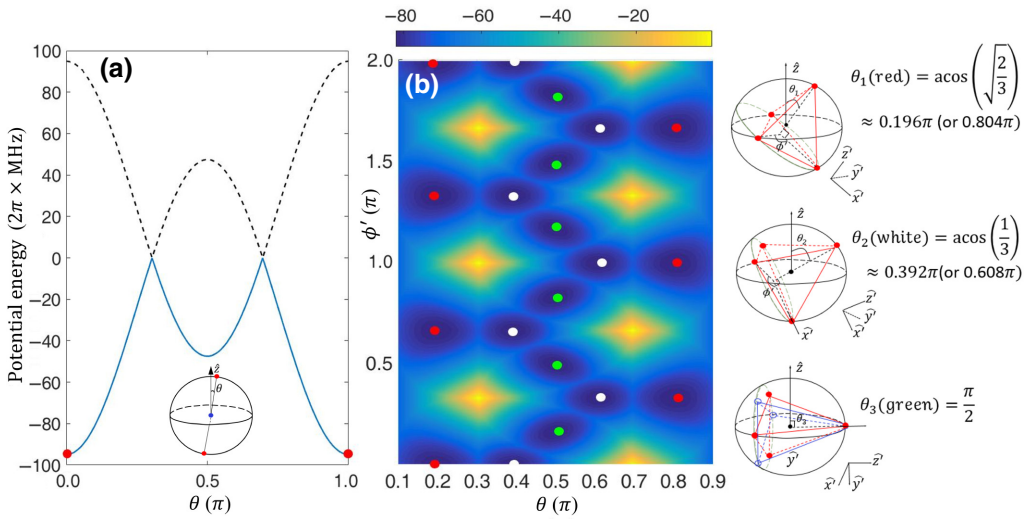


FIG. 6. Collective potential eigenenergies E_{\pm} and $E_{2,-}$ corresponding to (a) two and (b) four control atoms, versus the polarizing angle θ and the polarizing and azimuthal angles (θ, ϕ') , respectively. Subscript j is omitted for brevity. (b) In the case of four control atoms we introduce another angle ϕ' with respect to the rotational coordinate of $(\hat{x}', \hat{y}', \hat{z}')$, in order to determine the spatial position of atoms. On the right side of (b) we show three possible distributions of control atoms in a 3D sphere corresponding to red dots, white dots, and green dots, where the absolute value of potential energy $E_{2,-}$ attains its maximum.

with its eigenenergies explicitly as

$$\begin{aligned} E_{1,\pm} &= \frac{3B_4 \pm \sqrt{B_4^2 + 4D_4^2}}{4}, \\ E_{2,\pm} &= \frac{B_4 \pm \sqrt{B_4^2 + 216D_4^2}}{12}. \end{aligned} \quad (\text{D7})$$

However due to multiple adjustable parameters from four control atoms [there are overall eight degrees of freedom $(\theta_{1-4}, \phi_{1-4})$ in the bare spherical coordinate] it is difficult to find out its maximal magnitude, which corresponds to a maximal asymmetric interaction. By considering the symmetry of potentials we guess a regular-tetrahedron structure. As displayed in Fig. 6(b)(right inset) an optimal regular-tetrahedron configuration is freely rotated in which the polarizing angle θ (denoted by $\theta_1, \theta_2, \theta_3$) with respect to one control atom (vertex) varies from 0 to $\pi/2$. Note that the range of $\theta \in (\pi/2, \pi)$ is equivalent due to the symmetry so we focus on $\theta \in (0, \pi/2]$. Besides, ϕ' is an azimuthal angle in the bottom side of tetrahedron, which is opposite to the vertex. With tunable θ and ϕ' , we show the potential energy $E_{2,-}$ in Fig. 6(b) where its maximal (absolute) values are denoted by dots. Periodical patterns along the ϕ' axis are explicitly observed due to the isotropy of three atoms in the bottom side. However, only at $(\theta_1, \theta_2, \theta_3) = (\arccos(\sqrt{2}/3), \arccos(1/3), \pi/2)$, the absolute value of $E_{2,-}$, which is $\propto |D_4|$ can reach its global maximum, corresponding to the optimal configurations as displayed on the right side of Fig. 6(b). Note that for $\theta_3 = \pi/2$ there exists

two types of bottom-side atomic distributions due to the periodicity.

To obtain a maximal asymmetric blockade among the cases of θ_1, θ_2 , and θ_3 , we analyze the ratio χ_j of each control atom and find that its minimum is $\min(\chi_j) \approx 828.44$ when $\theta = \theta_1$ (case 1). And this value lowers to 552.30 if $\theta = \theta_2$ (case 2). Case 3 with $\theta = \theta_3$ has an equivalent structure as the former case 2. Relevant parameters estimated in calculation are $C_3/2\pi = 4.194 \text{ GHz } \mu\text{m}^3$, $C_6/2\pi = -12 \text{ GHz } \mu\text{m}^6$, and $R_{ct} = 5.0 \mu\text{m}$. These results explicitly suggest that case 1 has the best asymmetry, which agrees with the optimal structure obtained by the evolutionary algorithm, see Fig. 1 ($n = 4$).

APPENDIX E: GATE IMPLEMENTATION

In the section we demonstrate how to realize a C_n NOT gate via asymmetric blockade. Consider ^{87}Rb atoms trapped in a 3D spheroidal array with $R_{ct} = 5.0 \mu\text{m}$. Qubit-state preparation depends on two hyperfine ground states $|0_{j,l}\rangle = |5S_{1/2}, F = 1, m_F = 0\rangle$ and $|1_{j,l}\rangle = |5S_{1/2}, F = 2, m_F = 0\rangle$ via an optically pumping method [71]. In practice the control atoms are globally driven via an one-step UV excitation from $|0_j\rangle$ to $|p_j\rangle = |60P_{3/2}\rangle$ with wavelength 297 nm; and the target atom will face a two-photon transition from $|0_t\rangle$ to $|s_t\rangle = |61S_{1/2}\rangle$ with wavelengths 795 and 474 nm, decided by the selection rules. For the target atom the intermediate state, e.g., $|5P_{1/2}\rangle$ is safely discarded due to dispersive interactions, and state $|1_t\rangle$ is also coupled to $|s_t\rangle$ by the same mechanism.

A straightforward realization of the multiqubit C_n NOT gates should obey

$$|00 \dots 0 \dots \beta\rangle = e^{i\varphi}|00 \dots 0 \dots \beta\rangle$$

and $\underbrace{|11 \dots 1 \dots \beta\rangle}_n = |\underbrace{11 \dots 1 \dots \bar{\beta}}_n\rangle$ (E1)

with $\beta \in [0, 1]$ and $\bar{\beta} \equiv 1 - \beta$. We omit the subscripts t , j . The relative phase φ is tunable by external fields and here $\varphi = 0$. To describe the gate implementation, we note that when any control atom is initialized in state $|0_j\rangle$ the preexcitation of the control qubit(s) can induce a strong control-target exchange interaction, which blocks the subsequent excitation of the target atom. Only if all control atoms are in idle state $|1_j\rangle$ that are uncoupled with the laser fields, a complete state conversion mediated by $|s_t\rangle$ takes place between $|0_t\rangle$ and $|1_t\rangle$ of the target atom. In the scheme, a weak control-control interaction can facilitate an individual manipulation for the target atom by each control qubit, avoiding the control-control blockade.

As usual we apply a piecewise pulse sequence Ω_{1-5} comprising three fundamental steps [72]. (1) The incidence π pulse with Rabi frequency Ω_1 is globally applied to all control atoms, which allows a Rydberg excitation of $|0_j\rangle \rightarrow |p_j\rangle$. (2) A pair of π pulses, which include Ω_2 and Ω_3 (or Ω_3 and Ω_4), can generate a state swap for the target atom between $|0_t\rangle$ and $|1_t\rangle$ if all control atoms are idle in $|1_j\rangle$, obeying the routes of

$$\begin{aligned} |1_t\rangle &\xrightarrow{\Omega_2} |s_t\rangle \xrightarrow{\Omega_3} |0_t\rangle, \\ \text{or } |0_t\rangle &\xrightarrow{\Omega_3} |s_t\rangle \xrightarrow{\Omega_4} |1_t\rangle, \end{aligned} \quad (\text{E2})$$

which depends on its initial status $|1_t\rangle$ (or $|0_t\rangle$). (3) A $(-\pi)$ -pulse Ω_5 can finally return the Rydberg state $|p_j\rangle$ to $|0_j\rangle$ via a deexcitation process. In the main text we assume the Rabi frequencies with magnitudes $\Omega_c = |\Omega_{1,5}|$ and $\Omega_t = |\Omega_{2,3,4}|$ throughout the paper.

APPENDIX F: OTHER TECHNICAL ERRORS

In this section we first address the errors from imperfect experimental technique leading to unwanted laser amplitude and phase fluctuations. The infidelity of the C_6 NOT gate versus fluctuations of laser field amplitude is plotted in Fig. 7(a) in which the fluctuation $\delta\Omega_{c(t)}$ with respect to $\Omega_{c(t)}$ is estimated by a random number. In other words, the relative variation of laser Rabi frequency $\delta\Omega_{c(t)}/\Omega_{c(t)}$ can be randomly obtained from a range of $[-\delta_\Omega, \delta_\Omega]$. By increasing the value δ_Ω , from Fig. 7(a) we know that the gate infidelity has an apparent growth. For $\delta_\Omega = 0.1$ the infidelity of a 3D C_6 NOT gate is approximately 0.035 after an average of 500 measurements. Similarly we also study the robustness of gate against the variation of laser phases. We assume that the fluctuated laser phase $\phi_{c(t)}$ obeys a

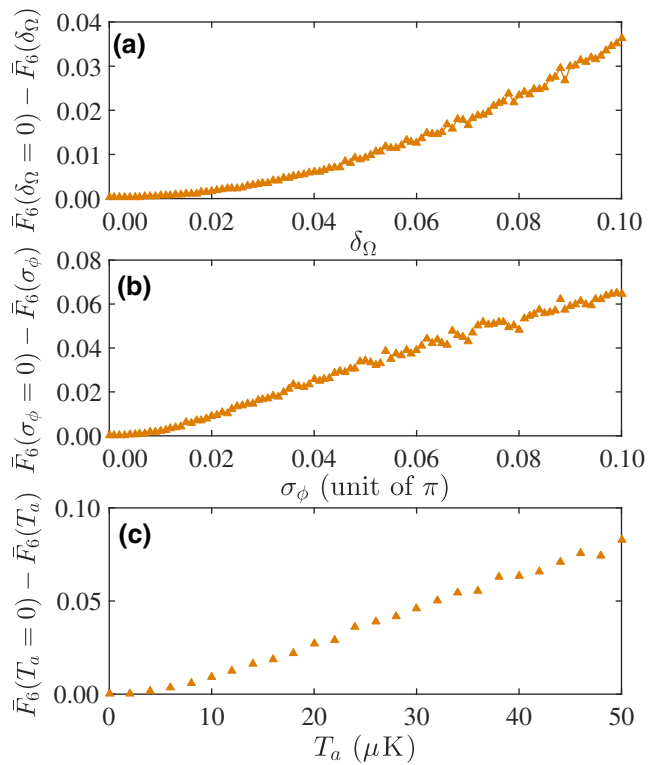


FIG. 7. Technical errors of a C_6 NOT gate caused by the imperfection of experimental conditions. (a),(b) Deviations in the laser amplitudes and phases. (c) Motional dephasing of atoms under different atomic temperatures. Every point represents an average over 500 measurements.

Gaussian distribution around the desired value $\phi_{c(t),0} = 0$ with the standard deviation $\sigma_\phi/\pi \in [0, 0.1]$. During each measurement a random laser phase $\phi_{c(t)}$ is adopted, which leads to $\Omega_{c(t)} \rightarrow \Omega_{c(t)}e^{i\phi_{c(t)}}$. From Fig. 7(b) we learn that the imperfection of gate fidelity also increases with the strength of phase fluctuation σ_ϕ . In fact once the laser amplitude or phase is fluctuated it would give rise to imperfect excitation or deexcitation during the process of state swap owing to the invalidity of π pulses [see Eq. (E2)], which will cause the gate inefficient.

Another inevitable technical error resource is the motional dephasing effect [73,74]. Due to the finite temperature, the thermal motion of control and target atoms will induce an inevitable Doppler dephasing to the excitation of Rydberg states, which can be estimated by a phase change to the laser Rabi frequencies

$$\Omega_t \rightarrow \Omega_t e^{i\Delta_{t,t}}, \Omega_c \rightarrow \Omega_c e^{i\Delta_{c,t}}, \quad (\text{F1})$$

where the detuning $\Delta_{t(c)}$ seen by the atoms satisfies a Gaussian distribution with its mean value $\bar{\Delta}_{t(c)} = 0$ and the standard deviation $\sigma_{\Delta_{t(c)}}$. Typically $\sigma_{\Delta_{t(c)}} = \mathbf{k}_{\text{eff}} \cdot \mathbf{v}$ where $\mathbf{k}_{\text{eff}} = \sum_j \mathbf{k}_j$ is the overall wavevector and $\mathbf{v} = v_{\text{rms}} = \sqrt{k_B T_a / M}$ is the atomic root-mean-square velocity with k_B ,

T_a , and M being the Boltzmann constant, atomic temperature, and atomic mass. To minimize the Doppler effect, for target atom, which undergoes a two-photon transition with wavelengths 795 and 474 nm the effective wavevector is $k_{t,\text{eff}} = (k_{474} - k_{495}) = 5 \times 10^6 \text{ m}^{-1}$ by considering two counterpropagating lasers, leading to $\sigma_{\Delta_t} = k_{t,\text{eff}} v_{\text{rms}}$ [75]. As for control atoms undergoing a one-step UV excitation $k_{t,\text{eff}} = k_{295} = 2 \times 10^7 \text{ m}^{-1}$ giving rise to $\sigma_{\Delta_c} = k_{c,\text{eff}} v_{\text{rms}}$. With these settings, in Fig. 7(c) we numerically calculate the imperfection of gate performance with respect to the temperature. For a given T_a we adopt a random detuning $\Delta_{t(c)}$ from the Gaussian function to simulate the phase error on the population evolution. By averaging over sufficient measurements we find the gate infidelity attains 0.08 at $T_a = 50 \mu\text{K}$ where the phase variations caused by atomic thermal motion are $\sigma_{\Delta_t} = 0.346 \text{ MHz}$, $\sigma_{\Delta_c} = 1.382 \text{ MHz}$, respectively.

-
- [1] E. Urban, T. A. Johnson, T. Henage, L. Isenhower, D. D. Yavuz, T. G. Walker, and M. Saffman, Observation of Rydberg blockade between two atoms, *Nat. Phys.* **5**, 110 (2009).
- [2] A. Gaëtan, Y. Miroshnychenko, T. Wilk, A. Chotia, M. Viteau, D. Comparat, P. Pillet, A. Browaeys, and P. Grangier, Observation of collective excitation of two individual atoms in the Rydberg blockade regime, *Nat. Phys.* **5**, 115 (2009).
- [3] S. Ravets, H. Labuhn, D. Barredo, L. Béguin, T. Lahaye, and A. Browaeys, Coherent dipole-dipole coupling between two single Rydberg atoms at an electrically-tuned Förster resonance, *Nat. Phys.* **10**, 914 (2014).
- [4] L. Isenhower, E. Urban, X. L. Zhang, A. T. Gill, T. Henage, T. A. Johnson, T. G. Walker, and M. Saffman, Demonstration of a Neutral Atom Controlled-NOT Quantum Gate, *Phys. Rev. Lett.* **104**, 010503 (2010).
- [5] D. Jaksch, J. I. Cirac, P. Zoller, S. L. Rolston, R. Côté, and M. D. Lukin, Fast Quantum Gates for Neutral Atoms, *Phys. Rev. Lett.* **85**, 2208 (2000).
- [6] M. D. Lukin, M. Fleischhauer, R. Cote, L. M. Duan, D. Jaksch, J. I. Cirac, and P. Zoller, Dipole Blockade and Quantum Information Processing in Mesoscopic Atomic Ensembles, *Phys. Rev. Lett.* **87**, 037901 (2001).
- [7] X. L. Zhang, L. Isenhower, A. T. Gill, T. G. Walker, and M. Saffman, Deterministic entanglement of two neutral atoms via Rydberg blockade, *Phys. Rev. A* **82**, 030306(R) (2010).
- [8] M. M. Müller, M. Murphy, S. Montangero, T. Calarco, P. Grangier, and A. Browaeys, Implementation of an experimentally feasible controlled-phase gate on two blockaded Rydberg atoms, *Phys. Rev. A* **89**, 032334 (2014).
- [9] M. Saffman, T. G. Walker, and K. Mølmer, Quantum information with Rydberg atoms, *Rev. Mod. Phys.* **82**, 2313 (2010).
- [10] M. A. Nielsen and I. L. Chuang, *Quantum Computation and Quantum Information: 10th Anniversary Edition* (Cambridge University Press, Cambridge, 2010).
- [11] C. Figgatt, D. Maslov, K. A. Landsman, N. M. Linke, S. Debnath, and C. Monroe, Complete 3-qubit grover search on a programmable quantum computer, *Nat. Commun.* **8**, 1918 (2017).
- [12] A. Saha, R. Majumdar, D. Saha, A. Chakrabarti, and S. Sur-Kolay, Asymptotically improved circuit for a d -ary Grover's algorithm with advanced decomposition of the n -qudit Toffoli gate, *Phys. Rev. A* **105**, 062453 (2022).
- [13] E. Brion, A. S. Mouritzen, and K. Mølmer, Conditional dynamics induced by new configurations for Rydberg dipole-dipole interactions, *Phys. Rev. A* **76**, 022334 (2007).
- [14] I. I. Beterov, I. N. Ashkarin, E. A. Yakshina, D. B. Tretyakov, V. M. Entin, I. I. Ryabtsev, P. Cheinet, P. Pillet, and M. Saffman, Fast three-qubit Toffoli quantum gate based on three-body Förster resonances in Rydberg atoms, *Phys. Rev. A* **98**, 042704 (2018).
- [15] T. G. Walker and M. Saffman, Consequences of Zeeman degeneracy for the van der Waals blockade between Rydberg atoms, *Phys. Rev. A* **77**, 032723 (2008).
- [16] A. Barenco, C. H. Bennett, R. Cleve, D. P. DiVincenzo, N. Margolus, P. Shor, T. Sleator, J. A. Smolin, and H. Weinsteiner, Elementary gates for quantum computation, *Phys. Rev. A* **52**, 3457 (1995).
- [17] M. Saeedi and M. Pedram, Linear-depth quantum circuits for n -qubit Toffoli gates with no ancilla, *Phys. Rev. A* **87**, 062318 (2013).
- [18] T. C. Ralph, K. J. Resch, and A. Gilchrist, Efficient Toffoli gates using qudits, *Phys. Rev. A* **75**, 022313 (2007).
- [19] N. Yu, R. Duan, and M. Ying, Five two-qubit gates are necessary for implementing the Toffoli gate, *Phys. Rev. A* **88**, 010304(R) (2013).
- [20] L. Biswal, D. Bhattacharjee, A. Chattopadhyay, and H. Rahaman, Techniques for fault-tolerant decomposition of a multicontrolled Toffoli gate, *Phys. Rev. A* **100**, 062326 (2019).
- [21] H. Levine, A. Keesling, G. Semeghini, A. Omran, T. T. Wang, S. Ebadi, H. Bernien, M. Greiner, V. Vuletić, H. Pichler, and M. D. Lukin, Parallel Implementation of High-Fidelity Multiqubit Gates with Neutral Atoms, *Phys. Rev. Lett.* **123**, 170503 (2019).
- [22] M. Li, F.-Q. Guo, Z. Jin, L.-L. Yan, E.-J. Liang, and S.-L. Su, Multiple-qubit controlled unitary quantum gate for Rydberg atoms using shortcut to adiabaticity and optimized geometric quantum operations, *Phys. Rev. A* **103**, 062607 (2021).
- [23] M. Khazali and K. Mølmer, Fast Multiqubit Gates by Adiabatic Evolution in Interacting Excited-State Manifolds of Rydberg Atoms and Superconducting Circuits, *Phys. Rev. X* **10**, 021054 (2020).
- [24] T. H. Xing, P. Z. Zhao, and D. M. Tong, Realization of nonadiabatic holonomic multiqubit controlled gates with Rydberg atoms, *Phys. Rev. A* **104**, 012618 (2021).
- [25] M. Saffman and K. Mølmer, Efficient Multiparticle Entanglement via Asymmetric Rydberg Blockade, *Phys. Rev. Lett.* **102**, 240502 (2009).
- [26] L. Isenhower, M. Saffman, and K. Mølmer, Multibit c_k not quantum gates via Rydberg blockade, *Quantum Inf. Process.* **10**, 755 (2011).
- [27] H.-Z. Wu, Z.-B. Yang, and S.-B. Zheng, Implementation of a multiqubit quantum phase gate in a neutral atomic ensemble via the asymmetric Rydberg blockade, *Phys. Rev. A* **82**, 034307 (2010).

- [28] S. L. Su, Rydberg quantum controlled-phase gate with one control and multiple target qubits, *Chinese Physics B* **27**, 110304 (2018).
- [29] J. T. Young, P. Bienias, R. Belyansky, A. M. Kaufman, and A. V. Gorshkov, Asymmetric Blockade and Multiqubit Gates via Dipole-Dipole Interactions, *Phys. Rev. Lett.* **127**, 120501 (2021).
- [30] S. L. Su, H. Z. Shen, E. Liang, and S. Zhang, One-step construction of the multiple-qubit Rydberg controlled-phase gate, *Phys. Rev. A* **98**, 032306 (2018).
- [31] X.-Q. Shao, A.-D. Zhu, S. Zhang, J.-S. Chung, and K.-H. Yeon, Efficient scheme for implementing an n -qubit Toffoli gate by a single resonant interaction with cavity quantum electrodynamics, *Phys. Rev. A* **75**, 034307 (2007).
- [32] J. D. Arias Espinoza, K. Groenland, M. Mazzanti, K. Schoutens, and R. Gerritsma, High-fidelity method for a single-step n -bit Toffoli gate in trapped ions, *Phys. Rev. A* **103**, 052437 (2021).
- [33] S. E. Rasmussen, K. Groenland, R. Gerritsma, K. Schoutens, and N. T. Zinner, Single-step implementation of high-fidelity n -bit Toffoli gates, *Phys. Rev. A* **101**, 022308 (2020).
- [34] D. Barredo, V. Lienhard, S. de Léséleuc, T. Lahaye, and A. Browaeys, Synthetic three-dimensional atomic structures assembled atom by atom, *Nature (London)* **561**, 79 (2018).
- [35] A. Kumar, T.-Y. Wu, F. Giraldo, and D. S. Weiss, Sorting ultracold atoms in a three-dimensional optical lattice in a realization of Maxwell's demon, *Nature (London)* **561**, 83 (2018).
- [36] Y. Wang, X. Zhang, T. A. Corcovilos, A. Kumar, and D. S. Weiss, Coherent Addressing of Individual Neutral Atoms in a 3D Optical Lattice, *Phys. Rev. Lett.* **115**, 043003 (2015).
- [37] D. Barredo, S. de Léséleuc, V. Lienhard, T. Lahaye, and A. Browaeys, An atom-by-atom assembler of defect-free arbitrary 2D atomic arrays, *Science* **354**, 1021 (2016).
- [38] M. Martinez-Dorantes, W. Alt, J. Gallego, S. Ghosh, L. Ratschbacher, Y. Völzke, and D. Meschede, Fast Nondestructive Parallel Readout of Neutral Atom Registers in Optical Potentials, *Phys. Rev. Lett.* **119**, 180503 (2017).
- [39] D. Ohl de Mello, D. Schäffner, J. Werkmann, T. Preuschhoff, L. Kohfahl, M. Schlosser, and G. Birk, Defect-Free Assembly of 2D Clusters of More Than 100 Single-Atom Quantum Systems, *Phys. Rev. Lett.* **122**, 203601 (2019).
- [40] C. Sheng, J. Hou, X. He, K. Wang, R. Guo, J. Zhuang, B. Mamat, P. Xu, M. Liu, J. Wang, and M. Zhan, Defect-Free Arbitrary-Geometry Assembly of Mixed-Species Atom Arrays, *Phys. Rev. Lett.* **128**, 083202 (2022).
- [41] X.-F. Shi, Single-site Rydberg addressing in 3D atomic arrays for quantum computing with neutral atoms, *J. Phys. B: At. Mol. Opt. Phys.* **53**, 54002 (2020).
- [42] L. G. D'yachkov, B. V. Zelener, A. B. Klyarfeld, and S. Y. Bronin, Dipole-dipole interaction between Rydberg atoms, *J. Phys.: Conf. Ser.* **774**, 012162 (2016).
- [43] L. Béguin, A. Vernier, R. Chicireanu, T. Lahaye, and A. Browaeys, Direct Measurement of the van der Waals Interaction between Two Rydberg Atoms, *Phys. Rev. Lett.* **110**, 263201 (2013).
- [44] N. Šibalić, J. Pritchard, C. Adams, and K. Weatherill, Arc: An open-source library for calculating properties of alkali Rydberg atoms, *Comput. Phys. Commun.* **220**, 319 (2017).
- [45] R. Cheng, C. He, Y. Jin, and X. Yao, Model-based evolutionary algorithms: A short survey, *Complex Intell. Syst.* **4**, 283 (2018).
- [46] K. Mølmer, Y. Castin, and J. Dalibard, Monte Carlo wavefunction method in quantum optics, *J. Opt. Soc. Am. B* **10**, 524 (1993).
- [47] T. E. Lee, H. Häffner, and M. C. Cross, Collective Quantum Jumps of Rydberg Atoms, *Phys. Rev. Lett.* **108**, 023602 (2012).
- [48] C.-Y. Guo, L.-L. Yan, S. Zhang, S.-L. Su, and W. Li, Optimized geometric quantum computation with a mesoscopic ensemble of Rydberg atoms, *Phys. Rev. A* **102**, 042607 (2020).
- [49] X.-Q. Shao, T.-Y. Zheng, C. H. Oh, and S. Zhang, One-step achievement of robust multipartite Greenberger-Horne-Zeilinger state and controlled-phase gate via Rydberg interaction, *J. Opt. Soc. Am. B* **31**, 827 (2014).
- [50] J.-L. Wu, Y. Wang, J.-X. Han, Y.-K. Feng, S.-L. Su, Y. Xia, Y. Jiang, and J. Song, One-step implementation of Rydberg-Antiblockade swap and controlled-swap gates with modified robustness, *Photon. Res.* **9**, 814 (2021).
- [51] S.-L. Su, Y. Gao, E. Liang, and S. Zhang, Fast Rydberg antiblockade regime and its applications in quantum logic gates, *Phys. Rev. A* **95**, 022319 (2017).
- [52] S. L. Su, F. Q. Guo, J. L. Wu, Z. Jin, X. Q. Shao, and S. Zhang, Rydberg antiblockade regimes: Dynamics and applications, *Europhys. Lett.* **131**, 53001 (2020).
- [53] A. Browaeys and T. Lahaye, Many-body physics with individually controlled Rydberg atoms, *Nat. Phys.* **16**, 132 (2020).
- [54] X.-F. Shi, Transition Slow-Down by Rydberg Interaction of Neutral Atoms and a Fast Controlled-NOT Quantum Gate, *Phys. Rev. Appl.* **14**, 054058 (2020).
- [55] D. B. Tretyakov, I. I. Beterov, E. A. Yakshina, V. M. Entin, I. I. Ryabtsev, P. Cheinet, and P. Pillet, Observation of the Borromean Three-Body Förster Resonances for Three Interacting Rb Rydberg Atoms, *Phys. Rev. Lett.* **119**, 173402 (2017).
- [56] R. Li, S. Li, D. Yu, J. Qian, and W. Zhang, Optimal Model for Fewer-Qubit CNOT Gates with Rydberg Atoms, *Phys. Rev. Appl.* **17**, 024014 (2022).
- [57] T. M. Graham, M. Kwon, B. Grinkemeyer, Z. Marra, X. Jiang, M. T. Lichtman, Y. Sun, M. Ebert, and M. Saffman, Rydberg-Mediated Entanglement in a Two-Dimensional Neutral Atom Qubit Array, *Phys. Rev. Lett.* **123**, 230501 (2019).
- [58] M. Marcuzzi, J. c. v. Minář, D. Barredo, S. de Léséleuc, H. Labuhn, T. Lahaye, A. Browaeys, E. Levi, and I. Lesanovsky, Facilitation Dynamics and Localization Phenomena in Rydberg Lattice Gases with Position Disorder, *Phys. Rev. Lett.* **118**, 063606 (2017).
- [59] X.-F. Shi and Y. Lu, Quantum gates with weak van der Waals interactions of neutral Rydberg atoms, *Phys. Rev. A* **104**, 012615 (2021).
- [60] S. Ebadi, T. T. Wang, H. Levine, A. Keesling, G. Semeghini, A. Omran, D. Bluvstein, R. Samajdar, H. Pichler, W. W. Ho, S. Choi, S. Sachdev, M. Greiner, V. Vuletić, and M. D. Lukin, Quantum phases of matter on a 256-atom programmable quantum simulator, *Nature (London)* **595**, 227 (2021).

- [61] X. L. Zhang, A. T. Gill, L. Isenhower, T. G. Walker, and M. Saffman, Fidelity of a Rydberg-blockade quantum gate from simulated quantum process tomography, *Phys. Rev. A* **85**, 042310 (2012).
- [62] D. Paredes-Barato and C. S. Adams, All-Optical Quantum Information Processing using Rydberg Gates, *Phys. Rev. Lett.* **112**, 040501 (2014).
- [63] D. Petrosyan, F. Motzoi, M. Saffman, and K. Mølmer, High-fidelity Rydberg quantum gate via a two-atom dark state, *Phys. Rev. A* **96**, 042306 (2017).
- [64] K. M. Maller, M. T. Lichtman, T. Xia, Y. Sun, M. J. Piotrowicz, A. W. Carr, L. Isenhower, and M. Saffman, Rydberg-blockade controlled-NOT gate and entanglement in a two-dimensional array of neutral-atom qubits, *Phys. Rev. A* **92**, 022336 (2015).
- [65] X.-F. Shi, Rydberg Quantum Gates Free from Blockade Error, *Phys. Rev. Appl.* **7**, 064017 (2017).
- [66] M. Müller, I. Lesanovsky, H. Weimer, H. P. Büchler, and P. Zoller, Mesoscopic Rydberg Gate Based on Electromagnetically Induced Transparency, *Phys. Rev. Lett.* **102**, 170502 (2009).
- [67] X.-F. Shi, Fast, Accurate, and Realizable Two-Qubit Entangling Gates by Quantum Interference in Detuned Rabi Cycles of Rydberg Atoms, *Phys. Rev. Appl.* **11**, 044035 (2019).
- [68] T. J. Carroll, K. Claringbould, A. Goodsell, M. J. Lim, and M. W. Noel, Angular Dependence of the Dipole-Dipole Interaction in a Nearly One-Dimensional Sample of Rydberg Atoms, *Phys. Rev. Lett.* **93**, 153001 (2004).
- [69] A. Reinhard, T. C. Liebisch, B. Knuffman, and G. Raithel, Level shifts of rubidium Rydberg states due to binary interactions, *Phys. Rev. A* **75**, 032712 (2007).
- [70] H. Zoubi, A. Eisfeld, and S. Wüster, van der Waals–stabilized Rydberg aggregates, *Phys. Rev. A* **89**, 053426 (2014).
- [71] S. Kim and A. M. Marino, Generation of ^{87}Rb resonant bright two-mode squeezed light with four-wave mixing, *Opt. Express* **26**, 33366 (2018).
- [72] X.-F. Shi, Quantum logic and entanglement by neutral Rydberg atoms: Methods and fidelity, *Quantum Sci. Technol.* **7**, 023002 (2022).
- [73] X.-F. Shi, Suppressing Motional Dephasing of Ground-Rydberg Transition for High-Fidelity Quantum Control with Neutral Atoms, *Phys. Rev. Appl.* **13**, 024008 (2020).
- [74] S. de Léséleuc, D. Barredo, V. Lienhard, A. Browaeys, and T. Lahaye, Analysis of imperfections in the coherent optical excitation of single atoms to Rydberg states, *Phys. Rev. A* **97**, 053803 (2018).
- [75] D. Tiarks, S. Baur, K. Schneider, S. Dürr, and G. Rempe, Single-Photon Transistor using a Förster Resonance, *Phys. Rev. Lett.* **113**, 053602 (2014).